(Received 28 February 2024, Accepted 9 May 2024, Scheduled 22 May 2024)

Study on Electromagnetic Performance of Permanent Magnet Rotor and Dual Stator Starter Generator for Electric Vehicle Range Extender

Mingling Gao[1,*], Zhenhai Yu[1], Wenjie Jiao[2], Wenjing Hu[2],
Huihui Geng[2], Yixin Liu[2], Shiqiang Liu[2], and Yishuo Liu[2]

[1]*School of Computer Science and Technology, Shandong University of Technology, Zibo 255000, China*
[2]*School of Transportation and Vehicle Engineering, Shandong University of Technology, Zibo 255000, China*

ABSTRACT: The flywheel-type dual-stator permanent magnet starter generator combines engine flywheel and starter generator rotor into a single unit, which has the advantages of high efficiency, high power density, and compact structure. This paper proposes a new type of dual-stator permanent magnet starter generator topology in which the two stators are concentric and share the same permanent magnet rotor. Equivalent magnetic circuit modeling of the inner stator's magnetic field, outer stator's magnetic field, and synthetic magnetic field using the equivalent magnetic circuit method list the system of flux equations and solve the main magnetic flux, leakage flux, and leakage coefficient, and the results show that the equivalent magnetic circuit method has smaller error and higher accuracy than the finite element method. The harmonic electric potential of the starter generator is modeled and analyzed. The permanent magnet rotor and inner and outer stator structures are optimized to obtain the optimal parameters, and the prototype is manufactured and tested. The optimized starter generator no-load induced electromotive force fundamental amplitude is improved. The induced electromotive force harmonic distortion rate is reduced, and the output performance of the whole generator is significantly improved.

1. INTRODUCTION

The widespread use of automobiles has exacerbated the depletion of petroleum resources. In order to solve the problems of energy shortage and environmental pollution, new energy vehicles have become the main development direction of today's automobile industry [1–4]. At present, the starter generators used for electric vehicles mainly include electro-excitation starter generator and permanent magnet starter generator. Electrically-excited starter generators use the energized excitation winding to generate a magnetic field, and the size of the magnetic field is adjusted by adjusting the excitation current, which has good magnetization characteristics, but there are problems such as large excitation loss and low efficiency; permanent magnet starter generators provide an excitation field by permanent magnets, which have the advantages of small size, light weight, low loss, high efficiency, etc. Permanent magnet starter generator is the main development of starter generators for range extenders [5–8]. In recent years, dual-stator Permanent Magnet Generators (PMGs) have attracted much attention in the field of motor research because of their high output performance and high integration. Compared with the single-stator PM starter generator, double-stator PM starter generator adds a stator and a set of armature windings under the same volume, so it has higher power density and response speed [9–11]. Dual-stator PMG is a new type of motor with a special structure and working principle, which has important application value in the field of electric vehicles.

At present, many scholars have carried out in-depth research on double-stator permanent magnet motor. Scholars Wang et al. proposed a dual-stator hybrid excitation permanent magnet synchronous motor [12]. The machine consists of a radial stator, an axial stator, and a built-in tangential permanent magnet rotor. The permanent magnet has two flux paths, and the main flux of the radial magnetic field starts from the N-pole of the permanent magnet through the rotor core, passes through the radial main air gap, and returns to the S-pole of the permanent magnet through the radial stator core. The main flux of the axial magnetic field starts from the N-pole of the rotor sector block permanent magnet, passes through the axial air gap, and returns to the S-pole of the sector block permanent magnet through the axial stator, and the radial flux and axial flux form a parallel relationship. Zhao and Dong proposed an alternating pole dual stator permanent magnet starter generator [13]. The machine is a series magnetic circuit, consisting of an embedded "—" type alternating-pole permanent magnet rotor and two concentric stators. The alternating-pole structure reduces half of the permanent magnets, improves the utilization rate of permanent magnets in the whole machine, and ensures the output torque density of the motor. Zhao et al. proposed a dual-stator permanent magnet fault-tolerant motor [14]. The permanent magnet part and the reluctance part of the rotor are axially connected in parallel. This arrangement has better fault-tolerant perfor-

---

* Corresponding author: Mingling Gao (gml_3437@sina.com).

doi:10.2528/PIERB24022804

Published by THE ELECTROMAGNETIC ACADEMY

mance, stronger torque output capability, and overload capability. Gu proposed an anisotropic double-stator permanent magnet synchronous motor [15]. Unlike traditional double-stator motors, the anisotropic double-stator motor uses different numbers of poles for the inner and outer unit motors, which increases the torque density and also enables sensorless detection of the absolute motor position. Bilal et al. proposed a double stator axial flux spoke type permanent magnet motor [16]. This machine can effectively increase the air gap flux density and effective flux, require fewer ampere-turns to achieve the design requirements, and reduce the winding reactance, thus improving the power factor of this topology to some extent. Korean scholars Kim et al. proposed a dual-stator flux-switched permanent magnet motor [17] to replace the built-in permanent magnet synchronous motor in hybrid vehicles, which has a slider structure for the rotor and separate ferrite embedded in the inner and outer stators to make full use of the motor space. The motor increases the reluctance of the magnetic circuit compared with a single-stator flux-switched motor, solving the problem of oversaturation of the motor's magnetic chain, and the output torque is stable and smooth. Ahmad et al. proposed a surface-inserted double-stator permanent magnet synchronous motor [18]. The permanent magnets of this machine are surface-inserted structure, which can make full use of the reluctance torque generated by the asymmetry of the rotor magnetic circuit, and the internal and external double-surface-posted structure of the magnetic line of force mainly passes through the rotor core in the radial direction, which may not take into account the degree of saturation of the rotor core, and thus the rotor core can be designed thin enough to make full use of the internal space of the motor, as far as the strength of the mechanical structure permits. Tarek et al. and Wang et al. studied a new axial double stator "V" type built-in permanent magnet motor [19, 20]. Compared with the traditional surface-mounted axial flux motors, the structure of the machine to avoid the permanent magnets directly facing the air gap is prone to irreversible demagnetization compared with radial flux permanent magnet motor. Axial flux motor has the advantages of compact structure, high power density, wide range of speed change, etc., and the magnetic field of the main air gap is easy to adjust.

Combined with specific engineering applications, this paper proposes a new type of dual-stator permanent magnet starter generator, which needs to satisfy the requirements of providing a large starting torque at low speed in the starting state and outputting a stable voltage in the power generation state, in addition to meeting the space requirements of the starter generator installed between the engine and the flywheel, and therefore adopts a concentric dual-stator structure. The rotor structure is divided into surface-mounted and built-in types according to the different ways of placing the permanent magnets. Surface-mounted structure has a relatively weak ability to attenuate the magnetic field in order to expand the motor speed, and because the permanent magnets are directly facing the main air gap, it is easy to produce irreversible demagnetization. In contrast, the built-in structure of the permanent magnet is located inside the rotor core, which can reduce the irreversible demagnetization problem caused by the armature reaction, and the machine has higher power density and stronger overload capacity. According to the above analysis, the dual-stator permanent magnet starter generator designed in this paper have "V" type permanent magnets embedded in the outer side of the rotor, and the inner side of the rotor is surface-mounted permanent magnets, which is fixed by a pole shoe. The overall structure of the new dual stator permanent magnet starter generator is shown in Fig. 1, and the specification information is shown in Table 1.

TABLE 1. Technical indicator of double stator starter generator.

Starting Status Technical Indicators		Power Generation Status Technical Indicators	
Rated power	1.5 kW	Rated power	2 kW
Rated torque	14.3 N·m	Rated voltage	84 V
Rated speed	1000 r/min	Rated speed	4000 r/min

Compared with the traditional double stator starter generator with single pole structure, this machine adopts the rotor pole structure combining built-in and surface-mounted type, which improves the utilization rate of the rotor internal space, increases the power density and overload capacity of the motor, and increases the pole shoe on the outside of the surface-mounted permanent magnets so that they do not directly face the air gap, which reduces the irreversible demagnetization of permanent magnets due to the reaction of the armature and improves the reliability of the motor.

2. STARTER GENERATOR MAGNETIC CIRCUIT ANALYSIS

The magnetic field of permanent magnet starter generator for the internal and external double stator structure is distributed in the internal and external stator and permanent magnet rotor. The machine has three main magnetic flux magnetic circuits, and the main magnetic circuit distribution diagram is shown in Fig. 2. The three main magnetic flux paths of the starter generator pass through the middle part of the permanent magnet, and there are leakage fluxes at the two ends of the permanent magnet. In this paper, the leakage fluxes of the starter generator structure are mainly distributed at the two ends of the permanent magnet and the ends of the two neighboring permanent magnets, and a total of 7 leakage flux paths are obtained by analyzing the leakage flux magnetic paths. The leakage flux magnetic circuit distribution diagram of the starter generator is shown in Fig. 3, and the equivalent magnetic circuit diagram of magnetic circuit 1 is shown in Fig. 4.

Based on the magnetic circuit analysis, the equivalent magnetic circuit diagram of magnetic circuit 1 is plotted as shown in Fig. 4.

In Fig. 4, Φ_{pmv} is the magnetic flux of the "V" permanent magnet in magnetic circuit 1; Φ_{r1} is the magnetic flux of the rotor core magnetic circuit between the "V" permanent magnets in magnetic circuit 1; Φ_{lr1}, Φ_{lr2} and Φ_{lr3} are the leakage fluxes of the leakage circuit 1, leakage circuit 2, and leakage circuit 3, respectively,;and Φ_{rso} is the magnetic flux from the outside of the "V" shaped permanent magnet to the main air

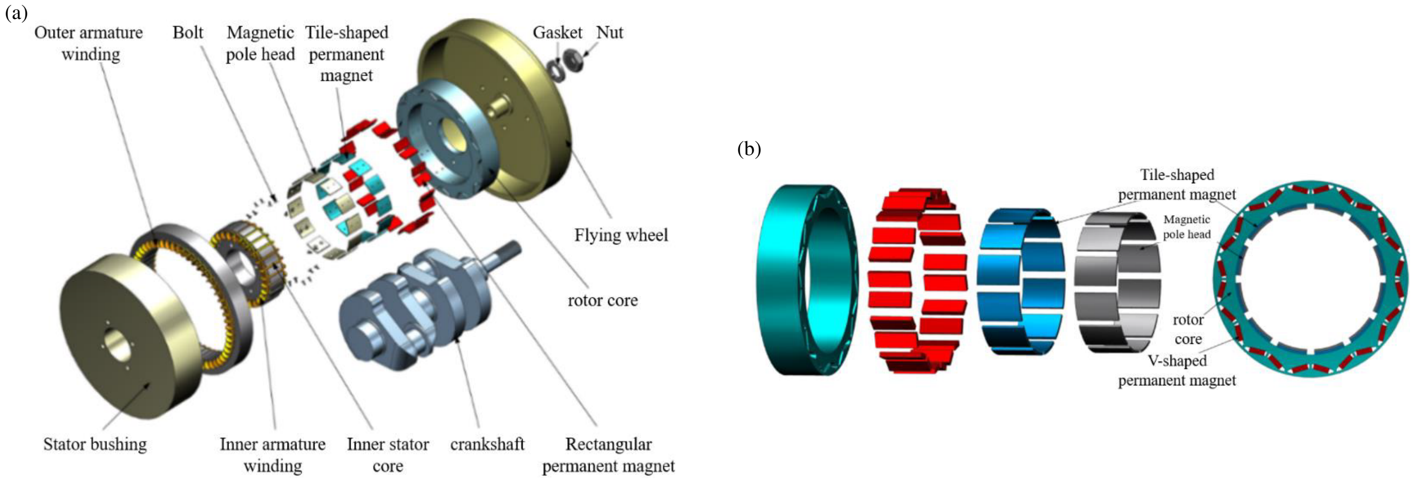

FIGURE 1. Structure of double stator permanent magnet starter generator. (a) Exploded view of the structure of a two-stator permanent magnet starter generator. (b) Topology diagram of permanent magnet rotor.

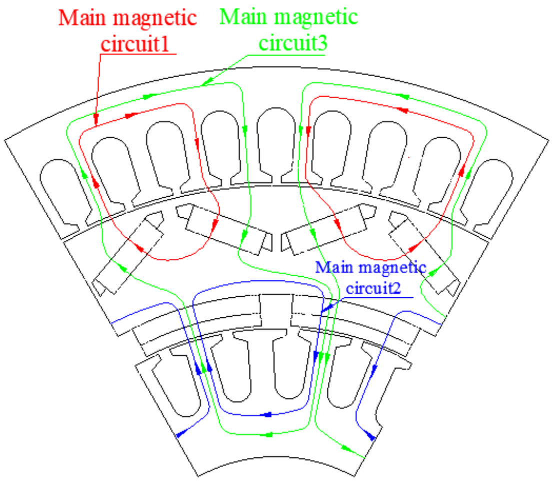

FIGURE 2. Distribution of the main magnetic circuit of the starter generator.

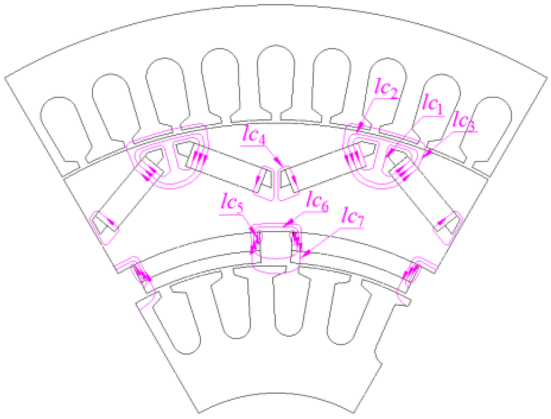

FIGURE 3. Leakage flux path distribution of starter generator.

gap portion of the magnetic circuit in magnetic circuit 1. Φ_{u1} is the effective magnetic flux of magnetic circuit 1. F_{pmv} is the magnetic kinetic potential generated by the "V" type permanent magnet in the magnetic circuit 1, and F_{ado1} is the magnetic kinetic potential of the straight-axis armature reaction in the magnetic circuit 1. The no-load condition is $F_{ado1} = 0$.

G_{pmv} is the internal permeability of the "V" permanent magnet, and $G_{pmv\delta}$ is the leakage permeability of the gap between the direction of the "V" permanent magnet's length and the rotor core. The leakage permeability between the rotor core and outer stator tooth slot in the leakage circuit 1 of the magnetic circuit 1 is G_{lr1}. The leakage permeability between the rotor core and outer stator tooth slot in the leakage circuit 2 of magnetic circuit 1 is G_{lr2}. The leakage permeability between the rotor core and outer stator tooth slot in the leakage circuit 3 of the magnetic circuit 1 is G_{lr3}. G_{r1} is the magnetic permeability of the rotor core magnetic circuit on the inside of the "V" type permanent magnet in magnetic circuit 1; G_{r2} is the magnetic permeability of the rotor core magnetic circuit on the outside of the "V" type permanent magnet; $G_{\delta o}$ is the magnetic permeability of the outer main air gap; and G_{sto} is the magnetic permeability of the outer stator magnetic circuit.

The equivalent magnetic circuit model of magnetic circuit 1 is solved using Kirchhoff's law for magnetic circuits, and points a, b, and c are taken as the flux calculation nodes in magnetic circuit 1. Four magnetic momentum calculation loops are computed for Loop 1, Loop 2, Loop 3, and Loop 4, and the set of flux equations for magnetic circuit 1 is:

$$\begin{cases} \Phi_{pmv} = \Phi_{r1} + \Phi_{lr1} \\ \Phi_{pmv} = \Phi_{lr1} + \Phi_{lr2} + \Phi_{rso} \\ \Phi_{rso} = \Phi_{lr3} + \Phi_{u1} \\ F_{pmv} = \Phi_{pmv} \left[\frac{1}{G_{pmv}} + \frac{2}{G_{pmv\delta}} \right] + \Phi_{lr1} \frac{1}{G_{lr1}} \\ +\Phi_{r1} \frac{1}{G_{r1}} - \Phi_{lr1} \frac{2}{G_{lr1}} + \Phi_{lr2} \frac{1}{G_{lr2}} = 0 \\ \Phi_{rso} \left[\frac{2}{G_{r2}} + \frac{2}{G_{\delta o}} \right] + \Phi_{lr3} \frac{1}{G_{lr3}} - \Phi_{lr2} \frac{1}{G_{lr2}} = 0 \\ \Phi_{u1} \frac{1}{G_{sto}} - F_{ado1} - \Phi_{lr3} \frac{1}{G_{lr3}} = 0 \end{cases} \tag{1}$$

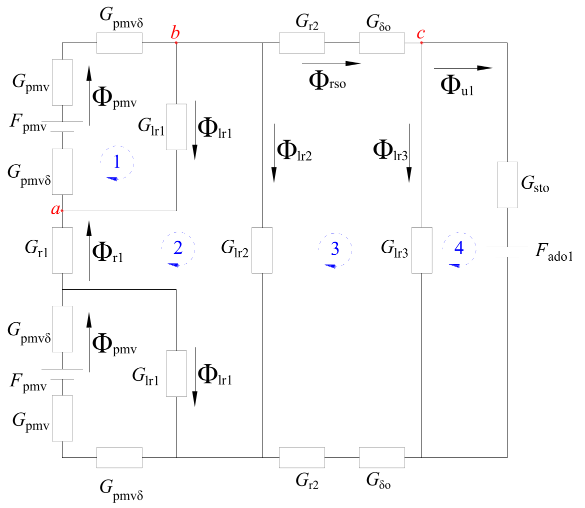

FIGURE 4. Equivalent magnetic circuit diagram of magnetic circuit 1.

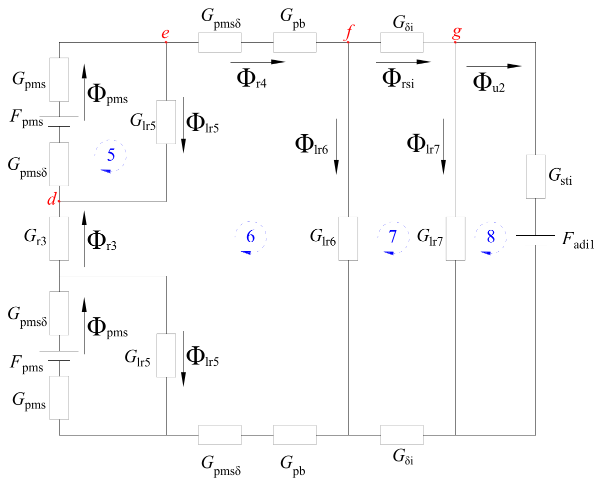

FIGURE 5. Equivalent magnetic circuit diagram of magnetic circuit 2.

Based on the magnetic circuit analysis, the equivalent magnetic circuit diagram of magnetic circuit 2 is plotted as shown in Fig. 5.

In Fig. 5, Φ_{pms} is the magnetic flux of the tile-shaped permanent magnet in magnetic circuit 2; Φ_{r3} is the magnetic flux of the outer rotor core magnetic circuit of the two tile-shaped permanent magnets in magnetic circuit 2; Φ_{lr5}, Φ_{lr6} and Φ_{lr7} are the leakage fluxes of the leakage circuit 5, leakage circuit 6, and leakage circuit 7, respectively, in magnetic circuit 2. Φ_{rsi} is the flux of the inner part of the tile-shaped permanent magnet to the main air gap part of the magnetic flux in magnetic circuit 2, and Φ_{u2} is the effective flux of the magnetic circuit 2. F_{pms} is the magnetic kinetic potential produced by the tile-shaped permanent magnet in magnetic circuit 2; F_{adi1} is the magnetic potential of the straight-axis armature reaction in magnetic circuit 2; and in the no-load condition $F_{adi1} = 0$. G_{pms} is the internal magnetic permeability of the tile-shaped permanent magnet; $G_{pms\delta}$ is the leakage permeability of the gap between the length's direction of the tile-shaped permanent magnet and the rotor core and the gap between the tile-shaped permanent magnet and the pole shoe.

In the leakage circuit 5, G_{lr5} is the leakage permeability of the rotor core and the air gap portion of the end of the tile-shaped permanent magnet. In the leakage circuit 6, G_{lr6} is the leakage permeability in the gap circuit of the two tile-shaped permanent magnets. In the leakage circuit 7, G_{lr7} is the leakage permeability in the inner stator teeth and stator slot portion of the magnetic circuit; G_{r3} is the magnetic permeability of the inner rotor core magnetic circuit of the two tile-shaped permanent magnets in the magnetic circuit 2; G_{pb} is the magnetic permeability of the pole shoe portion of the magnetic circuit; $G_{\delta i}$ is the magnetic permeability of the inner main air gap; and G_{sti} is the magnetic permeability of the inner stator magnetic circuit.

The equivalent magnetic circuit model of magnetic circuit 2 is solved using Kirchhoff's law for magnetic circuits, and points d, e, f, and g are taken as magnetic flux calculation nodes in magnetic circuit 2. A total of four magnetic momentum calculation loops are computed for Loop 5, Loop 6, Loop 7, and Loop 8, and the set of flux equations for magnetic circuit 2 is:

$$\begin{cases} \Phi_{pms} = \Phi_{r3} + \Phi_{lr5} \\ \Phi_{pms} = \Phi_{r4} + \Phi_{lr5} \\ \Phi_{r4} = \Phi_{rsi} + \Phi_{lr6} \\ \Phi_{rsi} = \Phi_{lr7} + \Phi_{u2} \\ F_{pms} = \Phi_{pms}\left(\frac{1}{G_{pms}} + \frac{1}{G_{pms\delta}}\right) + \Phi_{lr5}\,\frac{1}{G_{lr5}}\,\Phi_{r3}\,\frac{1}{G_{r3}} \\ -\Phi_{lr5}\,\frac{2}{G_{lr5}} + \Phi_{r4}\left(\frac{2}{G_{pms\delta}} + \frac{2}{G_{pb}}\right) + \Phi_{lr6}\,\frac{1}{G_{lr6}} = 0 \\ \Phi_{rsi}\,\frac{2}{G_{\delta i}} + \Phi_{lr7}\,\frac{1}{G_{lr7}} - \Phi_{lr6}\,\frac{1}{G_{lr6}} = 0 \\ \Phi_{u2}\,\frac{1}{G_{sti}} - F_{adi1} - \Phi_{lr7}\,\frac{1}{G_{lr7}} = 0 \end{cases} \tag{2}$$

Based on the magnetic circuit analysis, the equivalent magnetic circuit diagram of magnetic circuit 3 is plotted as shown in Fig. 6.

In Fig. 6, Φ_{r5} is the magnetic flux passing through the "V" type permanent magnet in the magnetic circuit 3; Φ_{lr4} is the magnetic flux of the leakage magnetic circuit 4 in the magnetic circuit 3; and Φ_{u3} is the effective magnetic flux of the magnetic circuit 3. In magnetic circuit 3, F_{adi2} is the straight-axis armature reactive magnetic potential generated by the outer stator's armature winding when no-load condition $F_{adi2} = 0$; F_{ado2} is the straight-axis armature reactive magnetic potential generated by the inner stator's armature winding, when no-load condition $F_{ado2} = 0$. G_{r4} is the permeability of the rotor core magnetic circuit between the "V" permanent magnet and the tile-shaped permanent magnet in magnetic circuit 3. In the magnetic circuit 3, G_{lr4} is the magnetic permeability of the rotor core portion of the magnetic circuit in the leakage circuit 4.

The equivalent magnetic circuit model of magnetic circuit 3 is solved using the magnetic circuit Kirchhoff's law, and the point h is taken as the magnetic flux calculation node in magnetic circuit 3. A total of four magnetic momentum calculation loops are calculated in loop 9 and loop 10, and the set of flux

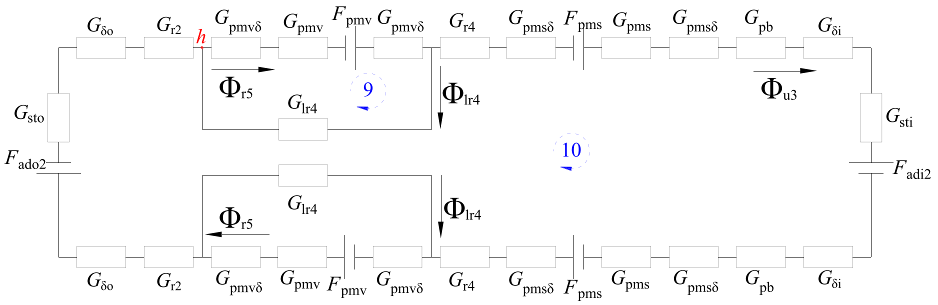

FIGURE 6. Equivalent magnetic circuit diagram of magnetic circuit 3.

equations for magnetic circuit 3 is:

$$\begin{cases} \Phi_{r5}-\Phi_{lr4}=\Phi_{u3} \\ F_{pmv}=\Phi_{r5}\left(\frac{1}{G_{pmv}}+\frac{2}{G_{pmv\delta}}\right)+\Phi_{lr4}\frac{1}{G_{lr4}}2F_{pms} \\ -\Phi_{lr4}\frac{2}{G_{lr4}}-F_{adi2}-F_{ado2}+\Phi_{u3} \\ \left(\begin{array}{l}\frac{1}{G_{pms}}+\frac{2}{G_{pms\delta}}+\frac{2}{G_{pb}}+\frac{2}{G_{\delta i}} \\ +\frac{1}{G_{sti}}+\frac{2}{G_{r4}}+\frac{2}{G_{r2}}+\frac{2}{G_{\delta o}}+\frac{1}{G_{sto}}\end{array}\right)=0 \end{cases} \tag{3}$$

By solving and calculating the three magnetic circuits, the electromagnetic characteristic parameters of the total magnetic field of the starter generator can be obtained. The effective magnetic flux per pole of the outer stator part of the starter generator is calculated as the sum of the effective flux of magnetic circuit 1 and the effective flux of magnetic circuit 3, and the effective magnetic flux per pole of the inner stator part is calculated as the sum of the effective flux of magnetic circuit 2 and the effective flux of magnetic circuit 3. The effective magnetic fluxes per pole of the outer stator and inner stator sections are respectively:

$$\Phi_{uo} = \Phi_{u1}+\Phi_{u3} \tag{4}$$

$$\Phi_{ui} = \Phi_{u2}+\Phi_{u3} \tag{5}$$

In the formulas Φ_{uo} is the effective magnetic flux per pole of the outer stator; Φ_{ui} is the effective magnetic flux per pole of the inner stator.

At the same time, the magnetic fields's leakage coefficients of the outer and inner stator sections are:

$$\sigma_o = \left(\Phi_{pmv}+\Phi_{r5}\right)/\Phi_{uo} \tag{6}$$

$$\sigma_i = \left(\Phi_{pms}+\Phi_{r5}\right)/\Phi_{ui} \tag{7}$$

The total leakage coefficient of the magnetic field of the starter generator is:

$$\sigma=\frac{\Phi_{pmv}+\Phi_{pms}+2\Phi_{r5}}{\Phi_{uo}+\Phi_{ui}} \tag{8}$$

To further calculate the magnitude of the magnetic flux of the starter generator, the finite element software field processor is utilized. A three-dimensional finite element simulation model of the starter generator is established, and the magnetic flux solution surface is drawn to solve the magnetic flux of each part of the starter generator. Draw a rectangular plane f_1 on the inside of the length direction of the "V" type permanent magnet to solve the magnetic flux generated by the "V" type permanent magnet; draw a circular plane f_2 on the outside of the tile-shaped permanent magnet to solve the magnetic flux generated by the tile-shaped permanent magnet; draw a surface f_3 for solving the magnetic flux per pole through the outer main air gap; similarly draw a surface f_4 for solving the magnetic flux per pole through the inner main air gap; draw a tangential rectangular plane f_5 between the outer center of the wedge-shaped spacer bridge on the outside of the "V" permanent magnet and the outer circle of the rotor core for solving the leakage flux in the rotor core at the outer end of the "V" shaped permanent magnet, that is, the leakage flux of the leakage circuit 1 and leakage flux of the leakage circuit 2. In order to solve the leakage flux of the leakage circuit 3, a tangential rectangular plane was drawn from the center of the slot wedge height of the external stator slot to the rotor outer circle. In order to solve the leakage flux in the leakage circuit 4, a radial rectangular plane was drawn in the center of the inner end isolated magnet bridge in the "V" type permanent magnet. In order to solve for the leakage flux at the end of the tile-shaped permanent magnet, a tangential rectangular plane was drawn from the center of the slot wedge height of the inner stator slot to the inner circle of the rotor. The leakage flux at the end of the tile-shaped permanent magnet is also the total magnetic flux of leakage circuit 5, leakage circuit 6, and leakage circuit 7. The starter generator flux solution surface and flux distribution are shown in Fig. 7 and Fig. 8.

According to the finite element magnetic flux calculation method, the magnetic flux density of each magnetic flux solution surface can be obtained by integrating the magnetic flux through each solution surface, and the finite element method of calculating each part of the magnetic flux and leakage flux with the equivalent magnetic circuit method calculation results are compared in Table 2.

Table 2 shows that the total magnetic flux and effective magnetic flux of the magnetic field where the inner and outer stators of the starter generator are located by the finite element method are slightly smaller than the results of the equivalent magnetic circuit method, with the maximum error not exceeding 1.5×10^{-5} Wb. The Leakage flux results from finite element calculations are slightly larger than those from equivalent magnetic circuit method calculations, but with the maximum error not exceeding 10^{-5} Wb, by the finite element method, the leakage coefficient of the magnetic field where the outer stators

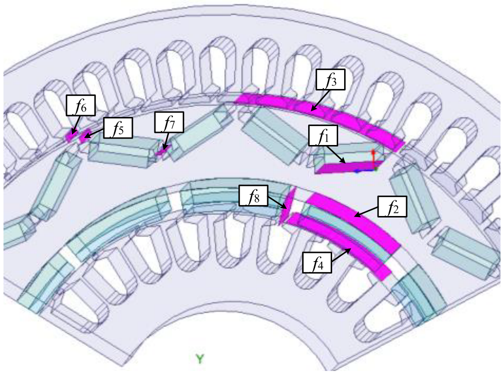

FIGURE 7. Starter generator flux solution surface.

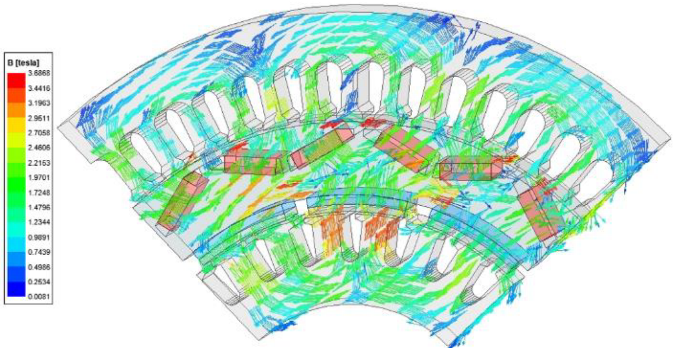

FIGURE 8. Starter generator flux distribution.

TABLE 2. Comparison of magnetic flux and leakage flux in each part calculated by the finite element method with the equivalent magnetic circuit method.

electromagnetic parameters	Finite element method calculation results/Wb	Equivalent Magnetic Circuit Method Calculations/Wb
Total flux of the magnetic field in which the outer stator is located	7.882×10^{-04}	7.996×10^{-04}
Total flux of the magnetic field in which the inner stator is located	6.537×10^{-04}	6.644×10^{-04}
Effective flux of the magnetic field in which the outer stator is located	6.098×10^{-04}	6.218×10^{-04}
Effective flux of the magnetic field in which the inner stator is located	5.615×10^{-04}	5.701×10^{-04}
Leakage flux in the rotor core at the outer end of the "V" shaped permanent magnet	1.262×10^{-04}	1.177×10^{-04}
Leakage flux of leakage circuit 3	6.345×10^{-07}	3.257×10^{-07}
Leakage flux of leakage circuit 4	5.499×10^{-05}	5.581×10^{-05}
Leakage flux at the end of a tile-shaped permanent magnet	3.873×10^{-05}	3.478×10^{-05}

are located is 1.295, slightly larger than that of the equivalent magnetic circuit method, 1.286.

The leakage coefficient of the magnetic field where the inner stator is located within the finite element method is calculated to be 1.164, which is slightly smaller than the 1.165 calculated by the equivalent magnetic circuit method. The finite element method calculates the leakage coefficient of the whole machine to be 1.232, which is slightly larger than the 1.228 calculated by the equivalent magnetic circuit method. However, the maximum error between the leakage coefficient calculated by the finite element method and the equivalent magnetic circuit method does not exceed 0.01, which is a small error. Overall comparison can be obtained, the electromagnetic characteristic parameters of the starter generator obtained by the finite element method are basically the same as those calculated by the equivalent magnetic circuit method, and the error is small, which verifies the validity of the equivalent magnetic circuit method.

3. HARMONIC ELECTROMOTIVE FORCE OPTIMIZATION ANALYSIS

Neglecting the stator slot wedge height and equating it to an open rectangular slot, the analytical expression for the permanent magnet field's main air-gap permeability $\lambda_\delta(x)$ is Fourier transformed and then [21–23] is calculated as:

$$\lambda_\delta(x) = \lambda_0 + \sum_{n=1}^{\infty} \lambda_n \cos\left(\frac{2n\pi}{t_s} x - x_{0n}\right) \tag{9}$$

In the formulas, λ_0 is the air gap permeability amplitude at the initial position; λ_n is the air gap permeability nth harmonic amplitude and is calculated as follows:

$$\lambda_n = \frac{2\mu_0}{n\pi}\left(\frac{1}{\delta_o} - \frac{1}{\delta_o + h_s}\right)\sin\frac{nZb_{t0}}{D_{o2}} \tag{10}$$

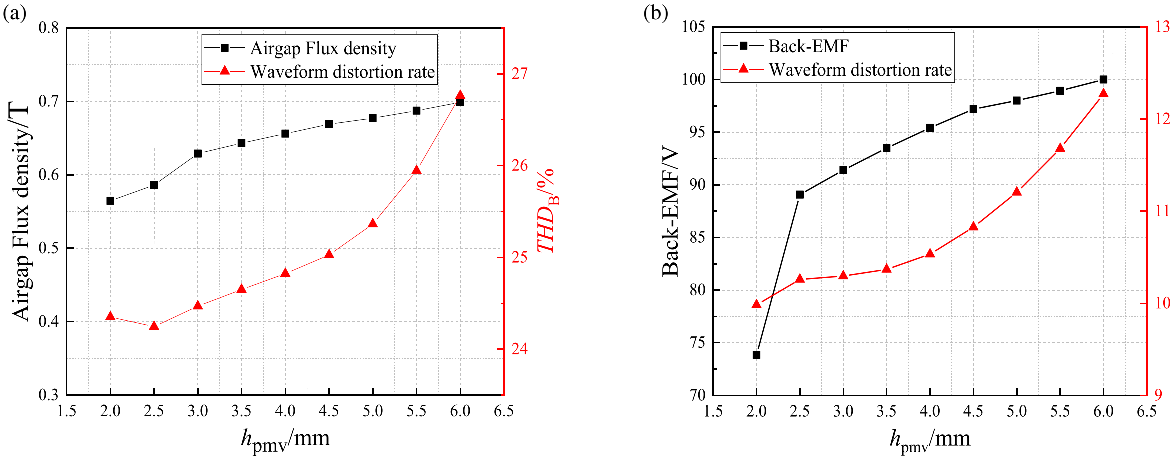

FIGURE 9. Variation curves of air gap density and induced electromotive force for different thicknesses in the magnetizing direction of "V" type permanent magnets. (a) Air-gap magnetic density fundamental amplitude and waveform distortion rate. (b) Induced electromotive force fundamental amplitude and waveform distortion rate.

In the formula, h_s is the height of the outer stator groove; b_{t0} is the width of the top of the outer stator teeth.

The magnetic flux generated by the permanent magnetic field enters the main air gap directly through the rotor, and the circumferential rotor magnetic kinetic potential $F_p(x)$ generated in the main air gap by the Fourier transform of the permanent magnetic field is:

$$F_p\left(x\right) = \sum_{n=1}^{\infty} F_n \sin\left(\frac{n\pi}{\tau_s} x\right) \quad n = 1, 3, 5, \cdots \tag{11}$$

In the formulas, F_n is the magnetic potential nth harmonic amplitude. τ_s is the Rotor pole width.

F_n is calculated as:

$$F_n = (-1)^{\frac{n+3}{2}} \frac{8B_r h_m}{n\pi\mu_r} \sin\left(\frac{n\pi\alpha}{2}\right) \tag{12}$$

In the formula, h_m is the length of permanent magnet magnetizing direction; α is the angle between the stator tooth centerline and the centerline of a specified pole.

The nth harmonic flux density of the permanent magnetic field B_{np} is calculated by circumferential resolution as:

$$\begin{aligned} B_n &= \lambda_n F_n = (-1)^{\frac{n+3}{2}} \frac{16\mu_0 B_r h_m}{\mu_p n^2 \pi^2} \\ &\times \left(\frac{1}{\delta} - \frac{1}{\delta + h_s}\right) \sin\left(\frac{n\pi\alpha}{2}\right) \sin\frac{nZb_{t0}}{D_{o2}} \end{aligned} \tag{13}$$

Collation yields the nth harmonic electric potential of the permanent magnet field e_{np}, and the analytical expression is:

$$\begin{aligned} e_n &= (-1)^{\frac{n+3}{2}} \cdot \frac{8\omega R_s N_s L_{ef} \mu_0 B_r h_m}{n^2 \pi^2 \mu_r} \sum_{k=1}^{N} \sin(n\tau - \alpha) \\ &\times \left(\frac{1}{\delta} - \frac{1}{\delta + h_s}\right) \sin\left(\frac{nZb_t}{D_{o2}}\right) \sin\left(\frac{n\pi\alpha}{2}\right) \end{aligned} \tag{14}$$

From Equation (14), it can be seen that after determining the permanent magnet material and the main structural dimensions of the starter generator, the main parameters affecting the harmonic electric potential of the permanent magnet field are the thickness of the permanent magnet magnet magnetizing direction, the length of the permanent magnet, and the stator slot parameters. Therefore, the permanent magnet size and stator slot parameters can be optimized to reduce the induced electric potential harmonics and improve the output performance of the starter generator.

3.1. Thickness of ``V'' Type Permanent Magnet Magnetizing Direction

Under the premise of ensuring that other parameters remain unchanged, the length of the "V" type permanent magnet magnetizing direction is taken as 2–6 mm, with a step size of 0.5 mm, and the simulation solves the change of the outer main air gap magnetization and induced electromotive force as shown in Fig. 9.

As can be seen in Fig. 9(a), with the increase of the thickness h_{pmv} in the magnetizing direction of the "V" type permanent magnet, the magnitude of the air-gap magnetic density fundamental waveform and the waveform distortion rate gradually increase, and the waveform distortion rate of the air-gap magnetic density rises rapidly when it is more than 4.5 mm. The thickness of "V" type permanent magnet is $4 \sim 4.5$ mm, which is suitable for magnetization direction, and the waveform aberration rate of air gap magnet is lower at this time. As can be seen in Fig. 9(b), the base wave amplitude of the induced electromotive force is similar to the base wave amplitude of the air gap magnetic density, and the growth rate gradually becomes flat. With the increase of the thickness of "V" type permanent magnet magnetizing direction, the induced electromotive force waveform aberration rate also increases gradually, when it is more than 4.5 mm, the induced electromotive force waveform aberration rate growth is more obvious. Therefore, the thick-

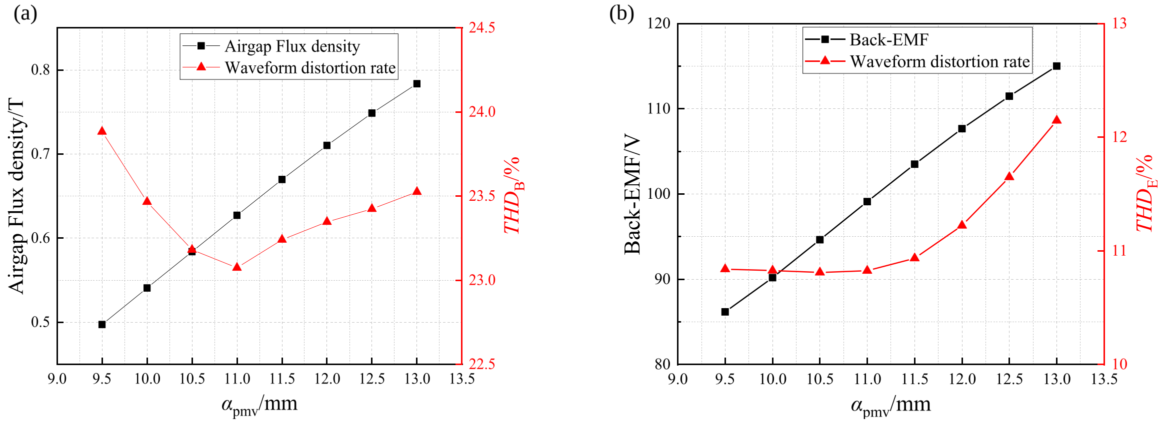

FIGURE 10. Variation curves of air gap density and induced electromotive force for different lengths of "V" type permanent. (a) Air-gap magnetic density fundamental amplitude and waveform distortion rate. (b) Induced electromotive force fundamental amplitude and waveform distortion rate.

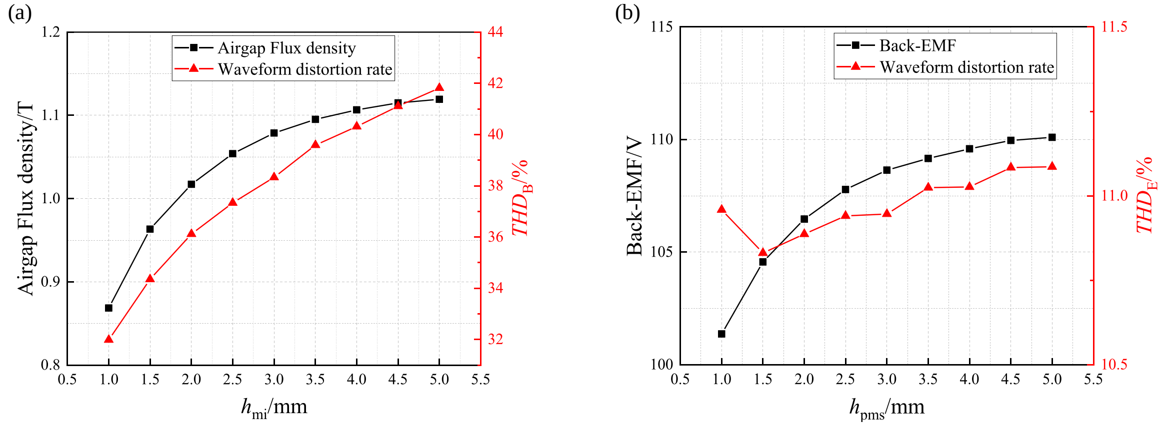

FIGURE 11. Air-gap magnetic density and induced electromotive force variation curves of different thicknesses in the magnetization direction of tile shaped permanent magnets. (a) Air-gap magnetic density fundamental amplitude and waveform distortion rate. (b) Induced electromotive force fundamental amplitude and waveform distortion rate.

ness of the "V" type permanent magnet in the magnetizing direction is 4.5 mm.

3.2. Length of ``V" Type Permanent Magnet

The length of the "V" permanent magnet is taken as 9–13 mm with a step of 0.5 mm, and the simulation solves for the outer main air gap and the induced electromotive force variation as shown in Fig. 10.

As can be seen in Fig. 10(a), with the increase of the length of the permanent magnet, the base wave amplitude of the air-gap magnetic density increases almost linearly, and the waveform distortion rate decreases gradually between 9.5 and 11 mm in the length of the "V" type permanent magnet. The minimum is achieved at 11 mm, and then the waveform distortion rate rises gradually after exceeding 11 mm. As can be seen in Fig. 10(b), with the increase of the length of the "V" type permanent magnet, the base wave amplitude of the induced electromotive force (EMF) increases linearly, and the no-load induced electromotive force (NED) waveform distortion rate rises rapidly after the length of the "V" type permanent magnet is increased to more than 11.5 mm. Combined with the influence of the length of the permanent magnet on the external main air-gap magnetic density, the length of the "V" type permanent magnet in this paper is taken as 12.5 mm.

3.3. Thickness in the Magnetizing Direction of Tile-Shaped Permanent Magnets

The thickness of the tile-shaped permanent magnet in the magnetizing direction is taken as 1–5 mm, and the step size is 0.5 mm, and the variation of the magnetic density and induced electromotive force of the main air gap within the simulation solution is shown in Fig. 11.

As can be seen in Fig. 11(a), with the increase of the thickness h_{pms} of the tile-shaped permanent magnet in the magnetization direction, the air-gap magnetic density fundamental amplitude and waveform distortion rate show an increasing trend, and the growth trend slows down gradually. With the increase of the thickness of the tile-shaped permanent magnet in the magnetizing direction, the air gap magnetic field tends to be gradually saturated; the change of the air-gap magnetic density is getting smaller and smaller; the thickness of the tile-shaped permanent magnet of 3 mm is suitable. As can be seen in Fig. 11(b),

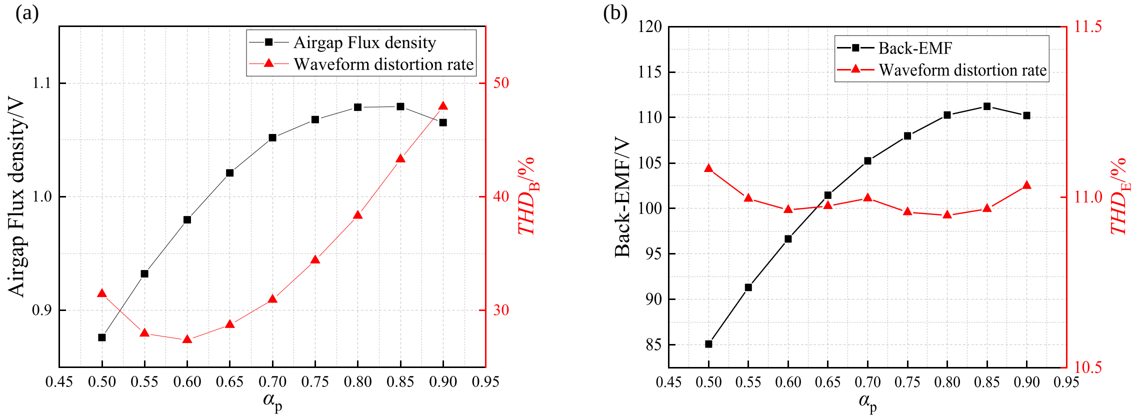

FIGURE 12. Variation curves of the airgap magnetic density and induced electromotive force with different pole-arc coefficients of tile-shaped permanent magnet poles. (a) Air-gap magnetic density fundamental amplitude and waveform distortion rate. (b) Induced electromotive force fundamental amplitude and waveform distortion rate.

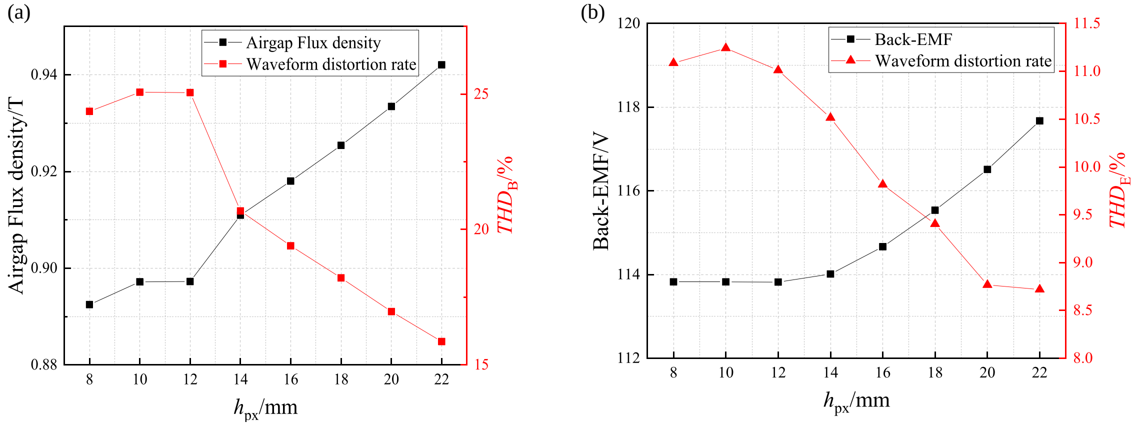

FIGURE 13. Variation curves of air-gap magnetic density and induced electromotive force for different eccentricity distances. (a) Air-gap magnetic density fundamental amplitude and waveform distortion rate. (b) Induced electromotive force fundamental amplitude and waveform distortion rate.

when the thickness of tile-shaped permanent magnet is between 1 and 2.5 mm, the base wave amplitude of induced electromotive force grows rapidly, and the growth tendency slows down gradually after it exceeds 2.5 mm, and the waveform distortion rate shows a more zigzagging change with the increase of the thickness of the magnetizing direction; therefore, the thickness of the tile-shaped permanent magnet is taken to be 3 mm.

3.4. Pole Arc Coefficients for Tile-Shaped Permanent Magnet Poles

The pole-arc coefficients of tile-shaped permanent magnet poles are taken from 0.5 to 0.9 with a step size of 0.05, and the variation of the main air-gap magnetic density and induced electromotive force within the simulation solution is shown in Fig. 12.

From Fig. 12(a), it can be seen that with the increase of the pole-arc coefficient, the air-gap magnetic density fundamental amplitude first rises, then decreases, and reaches the highest point when $\alpha_p = 0.8$, and for the waveform aberration rate, it shows a tendency to first decrease and then increase with the increase of the pole-arc coefficient. From Fig. 12(b), it can be seen that the base wave amplitude of the induced electromotive force first rises, then decreases, and achieves the peak value at 0.85, and the waveform distortion rate zigzags and changes, and achieves the minimum value at 0.8. When the polar arc coefficient is taken as 0.8, the starter generator has better output performance.

3.5. Eccentricity Distance of Rotor Outer Circle

Permanent magnet rotor eccentricity can change the outer main air gap axial structure and weaken the main air gap magnetization harmonic amplitude, which in turn affects the induced electromotive force harmonics. The rotor eccentricity is 8–22 mm, and the simulation step is 2 mm. The variation curves of magnetic density of the outer main air gap and induced electromotive force are obtained at different eccentricity distances by finite element simulation.

From Fig. 13(a), it can be seen that when the eccentricity is located between 12 and 22 mm, the air gap magnetization base wave amplitude increases at a faster rate, and after exceeding 16 mm, the waveform aberration rate basically shows a linear decreasing trend. From Fig. 13(b), it can be seen that the induced electromotive force (EMF) base wave amplitude gradually rises, and the waveform aberration rate exhibits the trend of rising and then decreasing. The decrease of the waveform aberration rate is obvious after exceeding 10 mm. After more than 20 mm, the waveform aberration rate decrease slows down. Therefore, the rotor eccentricity is taken as 20 mm.

3.6. Stator Optimization

In order to further improve the electromagnetic characteristics and output performance of the starter generator, the stator parameters are multiparameter optimized using Taguchi's algorithm. Since the inner stator's magnetic fields and outer stator's magnetic fields have little influence on each other, the inner stator's parameters and outer stator's parameters are optimized separately. Taguchi's method is a local optimization algorithm used to find the best combination of parameters to improve the quality of the product, which has the advantages of short computation period, simple establishment of objective function, and high efficiency [24]. The The flowchart of Taguchi algorithm is shown in Fig. 14.

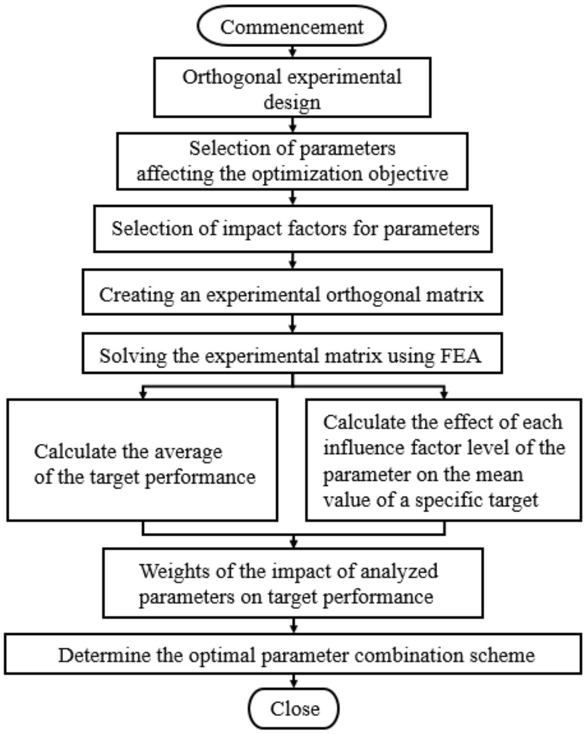

FIGURE 14. Flowchart of Taguchi optimization algorithm.

(1) Optimization objectives and optimization factors

According to the main influencing factors and quantitative objectives, this paper selects the no-load induced electromotive force fundamental amplitude $E_{\max}$, no-load induced electromotive force harmonic distortion rate THD_E, and air-gap magnetic density waveform distortion rate THD_B as the optimization objectives, b_{s0i}, b_{s1i}, b_{s2i}, h_{s1i} and h_{s2i} as the optimization parameters. Each parameter is selected as a factor level of five, and the experimental table of the optimization parameters and factor levels of the inner stator is shown in Table 3.

TABLE 3. Experimental table of optimized parameters and factor levels of the stator inside the dual-stator permanent magnet starter generator.

parameters	Level 1	Level 2	Level 3	Level 4	Level 5
b_{s0i}/mm	2.2	2.4	2.6	2.8	3
b_{s1i}/mm	5	5.5	6	6.5	7
b_{s2i}/mm	3.5	4	4.5	5	5.5
h_{s1i}/mm	0.6	0.8	1.1	1.2	1.4
h_{s2i}/mm	6	6.5	7	7.5	8

(2) Experimental design

According to the factors and levels in Table 3, the experimental matrix with the expression L25 (5^5) is established. If the traditional univariate, single-objective optimization method requires 3125 experiments, which is time-consuming and has heavy workload, the Taguchi algorithm is used to complete the optimization of the inner stator multi-parameter and multi-objective with only 25 experiments. The orthogonal test matrices of the influence factors of the inner stator parameters are established, and the experimental results are combined with the finite element method. The experimental orthogonal table and finite element solution results are shown in Table 4.

In order to analyze the effect of the changes in the optimization factors on the three optimization objectives, the average values of the experimental results in Table 4 are calculated [25, 26], and the average values of performance indicators are shown in Table 5:

$$M\left(S\right)=\frac{1}{n_s}\sum_{i}^{n_s}S_i=\frac{1}{25}\sum_{i=1}^{25}S\left(i\right) \tag{15}$$

In the formula n_s is the number of experiments; i is a constant, $i=1,2,3,\ldots,n_s$; S_i is the target mean of the ith experiment.

The average value of the performance index was calculated for each parameter factor:

$$M_{xi}=\frac{1}{4}\left[M_x\left(u_i\right)+M_x\left(v_i\right)+M_x\left(w_i\right)+M_x\left(o_i\right)\right] \tag{16}$$

In the formula, M_{xi} is the average value of the performance index under the ith optimization factor of the parameter; M_x is the performance index of the parameter under a particular test; u_i, v_i, w_i, o_i are experiment serial numbers.

The inner stator's induced electromotive force peak is $E_{\max}$. Induced electromotive force harmonic distortion rate THD_E and air-gap magnetic density harmonic distortion rate THD_B are represented by line graphs with the factor level variation curves, as shown in Fig. 15.

As can be seen from Fig. 15, the three groups of level combinations are designed for solving the optimal value of a single performance indicator, in order to comprehensively consider the impact of all performance indicators on the starter generator. It is now subjected to ANOVA analysis to determine the proportion of the impact of parameter changes on the performance indicators, and then to find the final optimization results,

TABLE 4. Experimental matrix and finite element analysis results of inner stator.

Ordinal number	Experimental Matrix					$E_{\max}$	THD_E	THD_B
	b_{s0i}/mm	b_{s1i}/mm	b_{s2i}/mm	h_{s1i}/mm	h_{s2i}/mm	V	%	%
1	1	1	1	1	1	33.69	1.61	29.63
2	1	2	2	2	2	32.26	2.98	31.79
3	1	3	3	3	3	30.15	5.37	34.51
4	1	4	4	4	4	27.64	8.11	37.59
5	1	5	5	5	5	24.48	11.84	41.46
6	2	1	2	3	4	32.14	4.18	31.81
7	2	2	3	4	5	30.18	6.58	34.48
8	2	3	4	5	1	29.58	7.24	35.39
9	2	4	5	1	2	27.69	7.56	38.35
10	2	5	1	2	3	29.26	4.95	36.72
11	3	1	3	5	2	31.58	5.51	32.70
12	3	2	4	1	3	30.08	6.70	34.98
13	3	3	5	2	4	27.22	10.04	38.67
14	3	4	1	3	5	30.18	6.18	35.10
15	3	5	2	4	1	28.89	7.40	37.08
16	4	1	4	2	5	29.48	8.79	35.64
17	4	2	5	3	1	28.82	9.63	36.69
18	4	3	1	4	2	31.82	5.38	32.77
19	4	4	2	5	3	29.89	7.77	35.54
20	4	5	3	1	4	28.35	7.08	37.94
21	5	1	5	4	3	28.11	11.25	37.60
22	5	2	1	5	4	31.52	6.58	32.97
23	5	3	2	1	5	31.09	6.10	33.80
24	5	4	3	2	1	30.24	6.81	35.11
25	5	5	4	3	2	27.54	10.20	38.83

TABLE 5. Table of average values of performance indicators.

Performance indicators	$E_{\max}$/V	THD_E/%	THD_B/%
$\bar{m}$	29.67	7.03	35.49

the variance expression is:

$$S\left(c\right)=\frac{1}{5}\sum_{i=1}^{5}\left[M_{xi}-M\left(c\right)\right]^2 \tag{17}$$

In the formula, S is each performance indicator; $S(c)$ is the variance of a performance indicator under parameter S; $M(c)$ is the average value of a performance indicator.

The variance and weight of the performance indexes for each parameter of the inner stator at 5 levels are shown in Table 6.

From the variance and specific gravity analyses, the induced electromotive force (EMF) fundamental amplitude $E_{\max}$ is maximized; the induced electromotive force (EMF) waveform distortion rate THD_E is minimized; the air-gap magnetic density harmonic distortion rate THD_B is minimized; and the final optimized factor level combinations are set as $b_{s0i}(1), b_{s1i}(1)$, $b_{s2i}(1), h_{s1i}(1)$, and $h_{s2i}(2)$, i.e., $b_{s0i}=2.2\,\text{mm}$, $b_{s1i}=5\,\text{mm}$, $b_{s2i}=3.5\,\text{mm}$, $h_{s1i}=0.6\,\text{mm}$, $h_{s2i}=6.5\,\text{mm}$.

In order to verify the electromagnetic characteristics of the inner stator of the double-stator permanent magnet starter generator before and after optimization, the optimization results obtained by the finite element method and Taguchi method are used for comparative analysis. A simulation analysis model is established using the optimized internal stator parameters, and the no-load induced electromotive force waveforms and the amplitudes of each harmonic of the internal stator of the double-stator PM starter generator before and after optimization are obtained as shown in Fig. 16.

From Fig. 16(a), it can be seen that the peak of the optimized induced electromotive force wave increases from 31.12 V to 34.56 V, while the waveform smoothness is improved. From Fig. 16(b) of the graph of the induced electromotive force amplitude of each harmonic, it can be seen that the optimized induced electromotive force fundamental amplitude increases from 28.5 V to 33.5 V, while the 2nd, 4th, 5th, 6th, 8th, and 9th harmonics are all reduced. The induced electromotive force waveform distortion rates before and after the optimization are calculated as 8.63% and 1.82%, respectively, and the in-

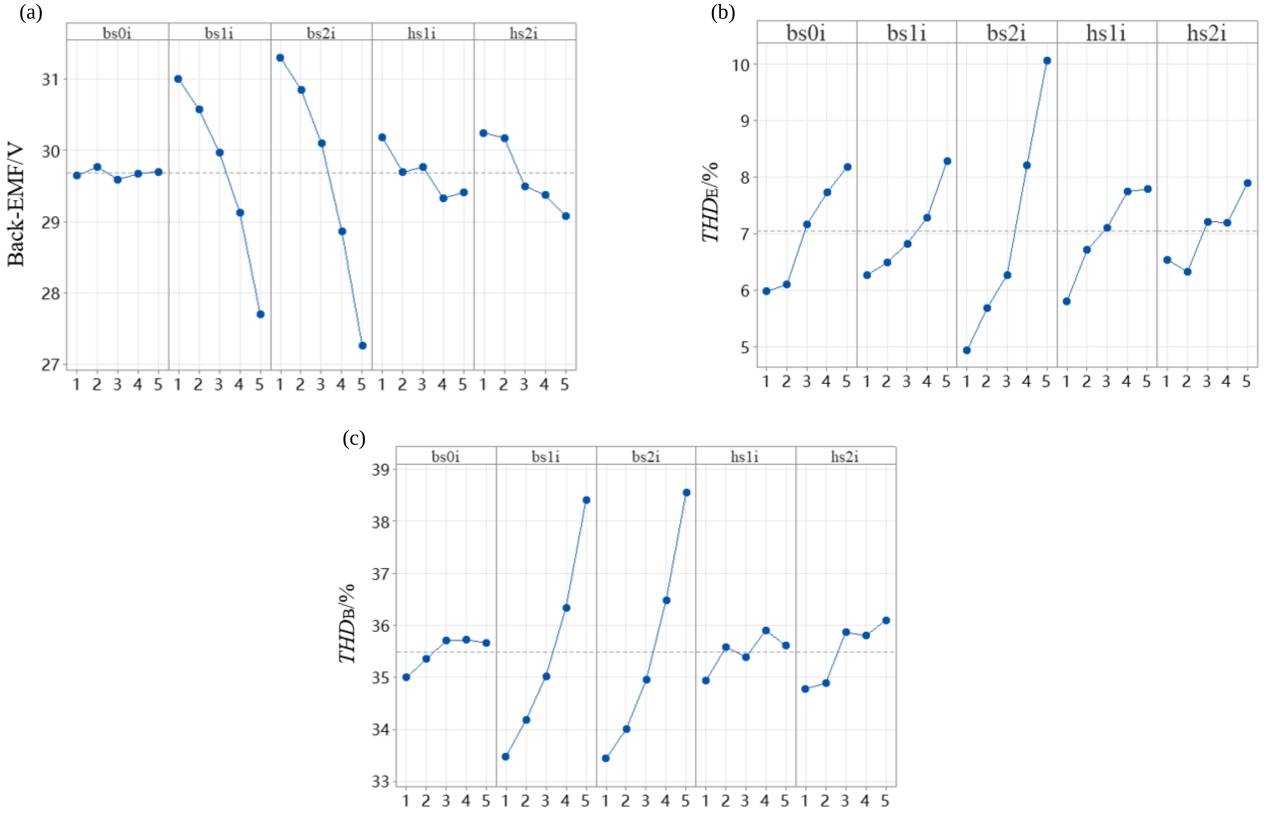

FIGURE 15. Line graph of the change of each index of inner stator with the level of factors. (a) Effects of factors on $E_{\max}$. (b) Effect of factors on THD_E. (c) Effect of factors on THD_B.

TABLE 6. Variance and weight of performance indexes for each parameter of inner stator at 5 levels.

parameters	$E_{\max}$		THD_E		THD_B	
	variance (statistics)	Specific gravity %	variance (statistics)	Specific gravity %	variance (statistics)	Specific gravity %
b_{si0}	0.00326	0.085818833	0.761192	13.61109656	0.078682	1.134204819
b_{si1}	1.36516	35.93755759	0.514093	9.192647141	3.038122	43.79467494
b_{si2}	2.13148	56.11077474	3.470692	62.06045772	3.421882	49.32659382
h_{si1}	0.08972	2.361860637	0.535983	9.584068627	0.103162	1.487085198
h_{si2}	0.20908	5.503988206	0.310477	5.551729952	0.295347	4.257441228
total value	3.7987	100	5.592437	100	6.937195	100

duced electromotive force waveform distortion rate decreases by 6.91% after the optimization.

The outer stator's structural parameters are analyzed and optimized. The no-load induced electromotive force fundamental amplitude $E_{\max}$, no-load induced electromotive force harmonic distortion rate THD_E, and inner air-gap density waveform distortion rate THD_B of the external stator are selected as the optimization objectives. The external stator slot structural parameters b_{s0o}, b_{s1o}, b_{s2o}, h_{s1o}, h_{s2o} are selected as the optimization parameters, and five factor levels are selected for analysis. The experimental table of outer stator optimization parameters and factor levels is shown in Table 7.

The line graph of the change of each index of the outer stator with the level of factors is shown in Fig. 17.

The variance and weight of the performance indexes for each parameter of the outer stator at 5 levels are shown in Table 8.

The analysis of the variance and weight of the performance indexes in Table 8 shows that the induced electromotive force (EMF) fundamental peak $E_{\max}$ is maximized; the induced electromotive force (EMF) waveform distortion rate THD_E is minimized; the air-gap magnetic density harmonic distortion rate THD_B is minimized, respectively; and the final optimized combination of the factor levels is set as $b_{s0o}(1)$, $b_{s1o}(1)$, $b_{s2o}(1)$, $h_{s1o}(4)$, and $h_{s2o}(3)$ which means that $b_{s0o} = 2.4$ mm, $b_{s1o} = 4.5$ mm, $b_{s2o} = 5.5$ mm, $h_{s1o} = 1.2$ mm, $h_{s2o} = 7$ mm.

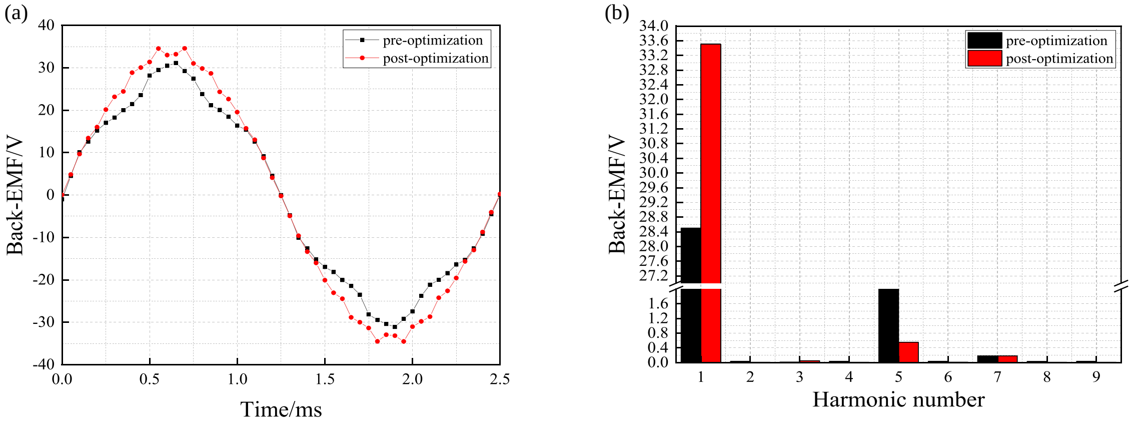

FIGURE 16. Waveforms of innner stator's induced electromotive force and amplitude of each harmonic before and after optimization. (a) Induced electromotive force waveform. (b) Comparison of the harmonics of the induced electromotive force.

TABLE 7. Experimental table of optimized parameters and factor levels of external stator for dual-stator PM starter generator.

parameters	Level 1	Level 2	Level 3	Level 4	Level 5
b_{s0o}/mm	2.4	2.6	2.8	3.0	3.2
b_{s1o}/mm	4.5	4.7	4.9	5.1	5.3
b_{s2o}/mm	5.5	5.8	6.1	6.3	6.5
h_{s1o}/mm	0.3	0.6	0.9	1.2	1.5
h_{s2o}/mm	6	6.5	7	7.5	8

TABLE 8. Variance and weight of performance indexes for each parameter of outer stator at 5 levels.

parameters	$E_{\max}$		THD_E		THD_B	
	variance (statistics)	Specific gravity %	variance (statistics)	Specific gravity %	variance (statistics)	Specific gravity %
b_{s0o}	0.12488	0.754684188	0.06366	1.570795441	0.23168	2.720696303
b_{s1o}	2.115939	12.78720136	0.094318	10.92824515	2.305783	12.13963009
b_{s2o}	13.44658	81.26138138	0.53369	66.7433461	6.742098	81.61072934
h_{s1o}	0.32428	1.959713232	0.036104	6.383179353	0.121098	2.159812041
h_{s2o}	0.53564	3.237019846	0.357187	14.37443395	0.14392	1.36913223
total value	16.547319	100	0.456011	100	8.868318	100

The no-load induced electromotive force waveforms and various harmonic amplitudes of the external stator of the double-stator permanent magnet starter generator before and after optimization, as well as the synthetic induced electromotive force and harmonic amplitudes before and after optimization are shown in Figs. 18 and 19, respectively.

From Fig. 18(a), it can be seen that the wave peak of the optimized outer stator's induced electromotive force is increased from 83.4 V to 85.9 V, while the waveform smoothness is improved, and from 18(b), it can be seen that the amplitude of the fundamental wave of the optimized induced electromotive force increases from 81.65 V to 85.07 V, while the 2nd, 4th, 6th, 7th, and 8th harmonics are all reduced, respectively. The induced electromotive force waveform distortion rates before and after optimization are 11.12% and 6.94%, which are reduced by 4.91% after optimization. From Fig. 19(a), it can be seen that the peak value of the synthetic induced electromotive force after optimization is improved, and the waveform is smoother. From the harmonic amplitude diagram in Fig. 19(b), it can be seen that the 3rd and 5th harmonics are obviously reduced after optimization, and the waveform distortion rate is reduced from 8.76% to 5.34%, which is a decrease of 3.42%. Through the analysis, it can be obtained that optimizing the stator slot size can effectively enhance the peak induced electromotive force of the starter generator, weaken the induced electromotive force harmonics, improve the waveform sinusoidality, and improve the output performance of the starter generator.

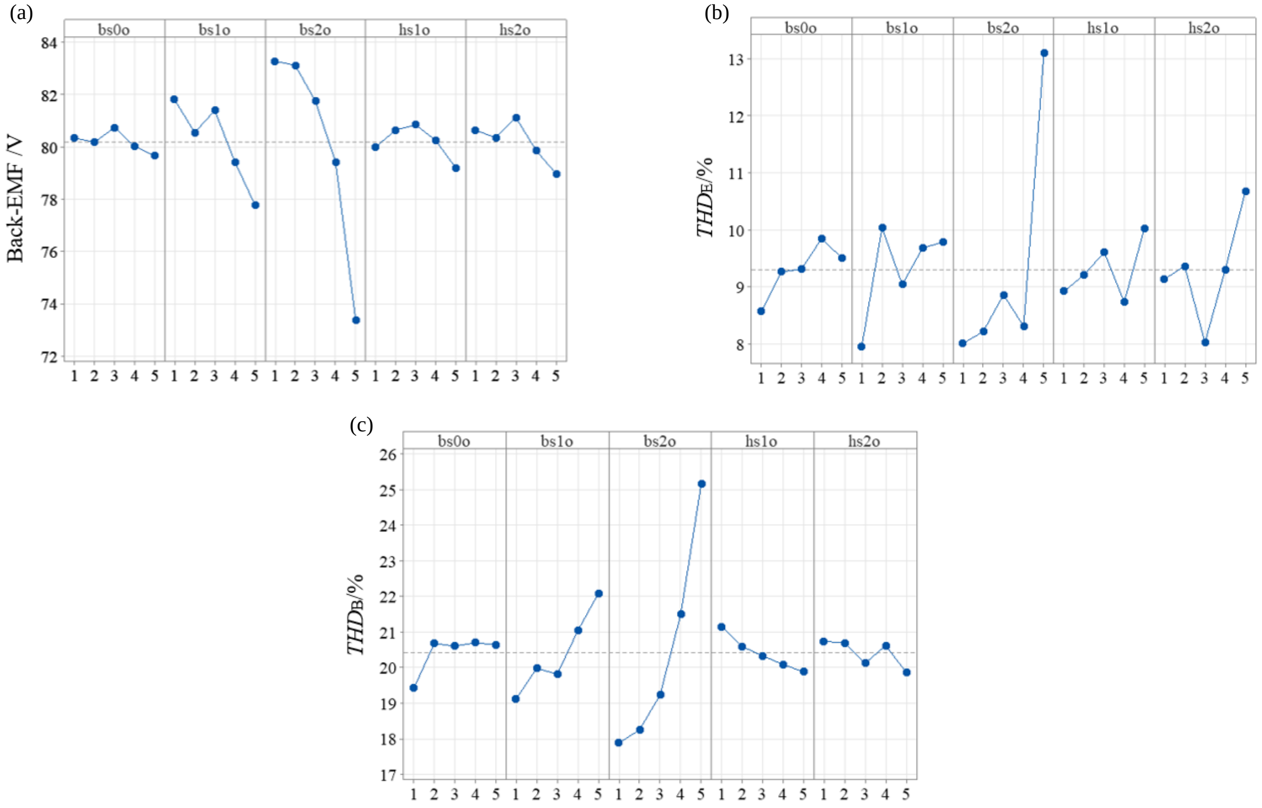

FIGURE 17. Line graph of the change of each index of outer stator with the level of factors. (a) Effect of factors on $E_{\max}$. (b) Effect of factors on THD_E. (c) Effect of factors on THD_B.

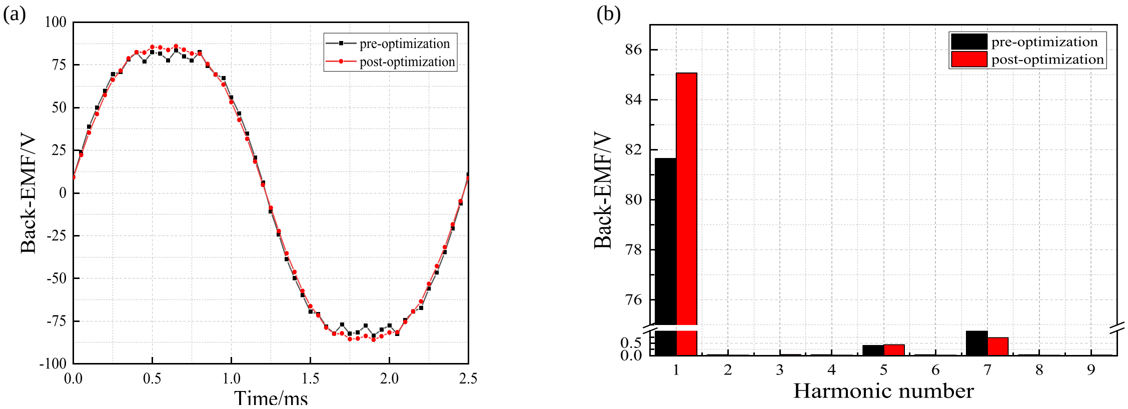

FIGURE 18. Waveforms of outer stator's induced electromotive force and amplitude of each harmonic before and after optimization. (a) Induced electromotive force waveform curve. (b) Comparison of the harmonics of the induced electromotive force.

TABLE 9. Structural parameters of double stator starter generator.

Structure parameter	Parameter values	Structure parameter	Parameter values
Poles	12	Number of outer stator slots	54
Diameter of Outer stator/mm	175	Number of Inner stator slots	27
Outer diameter of rotor core/mm	137	Outer air gap length/mm	0.5
Inner diameter of rotor core/mm	99	Inner air gap length/mm	0.5
Inner diameter of inner stator core/ mm	55	Silicon steel sheet model	DW310-35
Starter generator axial length/mm	30	Permanent magnet materials	NdFe35

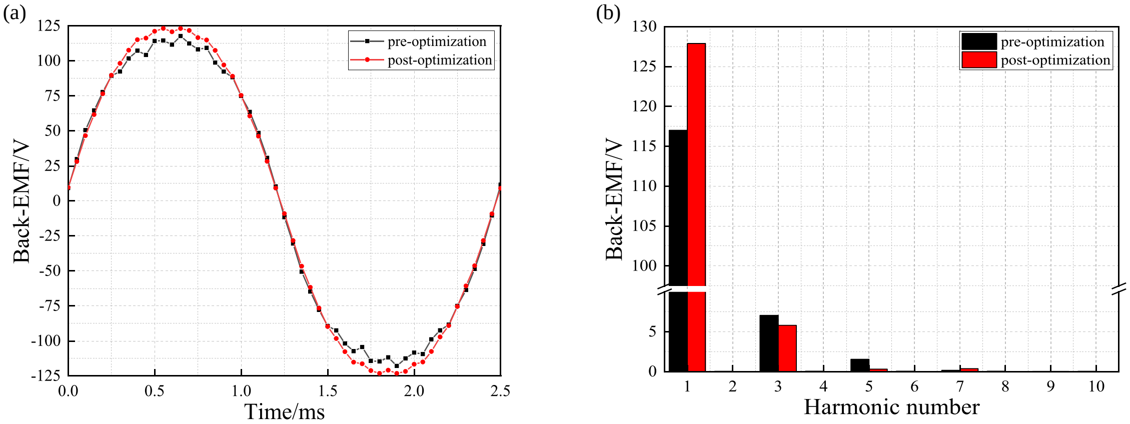

FIGURE 19. Synthesized induced electromotive force waveform and amplitude of each harmonic before and after optimization. (a) Induced electromotive force waveform curve. (b) Comparison of the harmonics of the induced electromotive force.

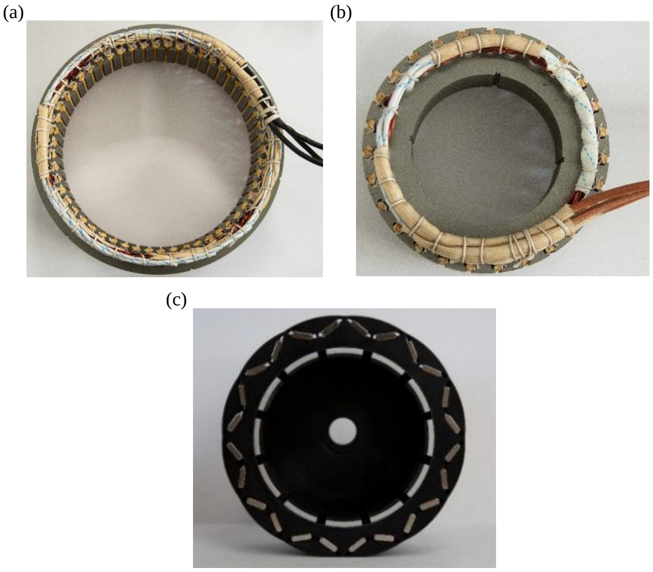

FIGURE 20. Stator core and rotor. (a) Outer stator. (b) Inner stator. (c) Permanent magnet rotor.

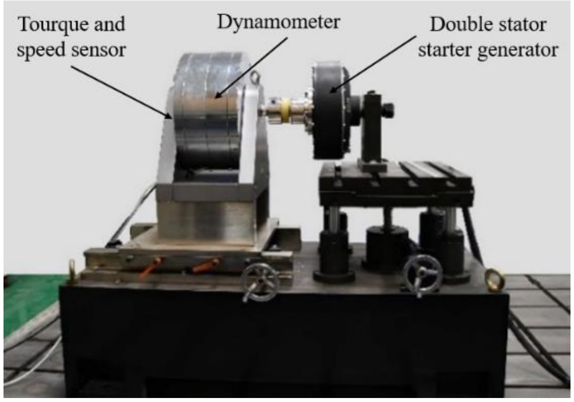

FIGURE 21. Experiment of double stator starter generator prototype platform.

4. PERFORMANCE EXPERIMENT

According to the optimized design parameters to develop a prototype of dual-stator permanent magnet starter generator, the main structural parameters of the prototype are shown in Table 9, and the stator core and rotor are shown in Fig. 20.

In order to verify the output performance of the dual-stator starter generator, an experimental platform is built, and a prototype test is carried out. The dual-stator starter generator test bed is shown in Fig. 21.

When the starter generator starts, the battery is connected to the starter controller, which leads to three wires that are connected to the three-phase armature windings of the double-stator starter generator. The crankshaft of the range extender engine is connected to the starter generator, and when the starting signal is given to the controller, the rotor of the starter generator will drive the crankshaft of the engine to rotate and complete the engine starting. The output performance characteristic points of the double stator PM starter generator starting condition are shown in Table 10.

As shown in Table 10, the output torque of the dual-stator permanent magnet starter generator at the rated point can reach 14.2 Nm; the maximum efficiency reaches 90.3%; and the output torque at full load condition reaches 29.6 Nm, which can satisfy the requirements of the starting engine conditions.

When the engine is running normally, the starter generator is converted to generator operation, which is driven by the engine to generate electrical energy, and the armature winding is connected to the voltage regulator controller to output a stable voltage. The waveform of no-load induced electromotive force at the rated speed of the starter generator is shown in Fig. 22.

As can be seen from Fig. 22, the no-load induced electromotive force waveform of the dual-stator permanent magnet starter generator is basically consistent with the finite element analysis results, and the peak induced electromotive force obtained experimentally is slightly smaller than that of the finite element results. The waveform distortion rates are 2.25% and 5.75%,

TABLE 10. Characteristic points of output performance for starting condition of dual-stator PM starter generator.

characteristic point	Current	Input power	Torque	Speed	Output power	Efficiency
rated point	21.62 A	1759 W	14.2 Nm	1022 r/min	1518 W	86.3%
Maximum power point	28.58 A	2320 W	29.6 Nm	664 r/min	2058 W	88.7%
peak efficiency point	27.40 A	2184 W	18.8 Nm	1002 r/min	1973 W	90.3%

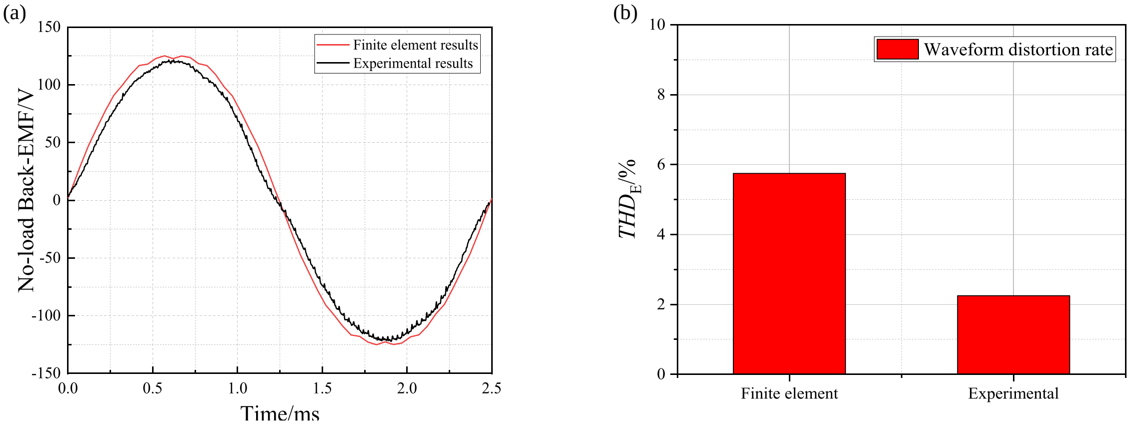

FIGURE 22. (a) No-load induced electromotive force waveform of starter generator. (b) Induced electromotive force waveform distortion rate.

TABLE 11. Performance test results of dual-stator permanent magnet starter generator.

Speed/(r/min)		2000			4000			4800	
Load power/W	1950	2000	2050	1950	2000	2050	1950	2000	2050
Output Voltage/V	83.4	83.2	82.7	84.8	84.5	84.3	85.1	84.9	84.8

respectively, and both of the induced electromotive force waveforms have a lower distortion rate, which indicates that the harmonics of the optimized starter generator are reduced, and the output performance is good.

The performance test of the double stator permanent magnet starter generator is carried out when the load power is 1950 W, 2000 W, 2050 W, and the rotational speed is 2000 r/min, 4000 r/min, 4800 r/min, respectively. The test results are shown in Table 11.

Table 11 shows that when the starter generator speed is 2000 r/min, and the load power increases from 1950 W to 2050 W, the maximum output voltage is 83.4 V, and the minimum is 82.7 V, which is slightly lower than the rated voltage. When the rotational speed is 4800 r/min, the maximum output voltage of the starter generator under different loads is 85.1 V, and the minimum is 84.8 V, which is slightly larger than the rated voltage. When the starter generator speed increases from 2000 r/min to 4800 r/min, and the load power increases from 1950 W to 2050 W, the output voltage can be stabilized between 82.7 V and 85.1 V. It can be seen that the starter generator voltage regulator controller can control the output voltage of starter generator to stabilize near the rated voltage under different speeds and load conditions, and the voltage regulator effect is good.

5. CONCLUSION

This paper proposes a concentric rotor, double stator permanent magnet starter generator structure with embedded "V" type permanent magnet on the outside and surface-mounted permanent magnet with pole shoe on the inside, and adopts the equivalent magnetic circuit method to analyze the magnetic field of the starter generator, establish a set of flux equations, and give a calculation method for the synthetic magnetic flux and leakage flux coefficient. The method is used to calculate the electromagnetic characteristic parameters of the magnetic field of the starter generator, and the magnetic flux and leakage flux of each part are obtained by combining with the finite element software, which are compared and analyzed with the equivalent magnetic circuit method, and the validity of the calculation results of the equivalent magnetic circuit method is verified. Through the analytical calculation of harmonic electric potential, the structural parameters affecting harmonic electric potential are determined; the influence law of rotor structural parameters on air gap magnetic density and induced electric potential is analyzed; and the Taguchi method is used to optimize the parameters of the inner and outer stators to further improve the amplitude of the fundamental wave of no-load induced electric potential, reduce the rate of harmonic aberration of the induced electric potential, and improve the electromagnetic performance and output performance of the whole machine. The test results show that the rated output torque of the double-stator PM starter generator is 14.2 Nm during the starting condition; the maximum efficiency reaches 90.3%; and the torque at the maximum power point is 29.6 Nm, which is able to meet the requirements of the starting condition of the starter generator. During the generating condition, the output voltage is stabilized between 82.7 V and 85.1 V under the conditions of variable speed and load, and the starter generator has good output performance.

ACKNOWLEDGEMENT

We acknowledge the support from the National Natural Science Foundation of China under Grant No. 52305267, and the Shandong Provincial Natural Science Foundation Grant No. ZR2023QE010.

REFERENCES

[1] Wang, X., X. He, and P. Gao, "Research on electromagnetic vibration noise attenuation method of permanent magnet motor with V-magnet rotor for electric vehicles," *Chinese Journal of Electrical Engineering*, Vol. 39, No. 16, 4919–4926+4994, 2019.

[2] Baek, S.-W. and S. W. Lee, "Design optimization and experimental verification of permanent magnet synchronous motor used in electric compressors in electric vehicles," *Applied Sciences*, Vol. 10, No. 9, 3235, 2020.

[3] Sun, X., Z. Shi, G. Lei, Y. Guo, and J. Zhu, "Analysis and design optimization of a permanent magnet synchronous motor for a campus patrol electric vehicle," *IEEE Transactions on Vehicular Technology*, Vol. 68, No. 11, 10 535–10 544, 2019.

[4] Yang, Y., Q. He, C. Fu, S. Liao, and P. Tan, "Efficiency improvement of permanent magnet synchronous motor for electric vehicles," *Energy*, Vol. 213, 118859, 2020.

[5] Agamloh, E., A. V. Jouanne, and A. Yokochi, "An overview of electric machine trends in modern electric vehicles," *Machines*, Vol. 8, No. 2, 20, 2020.

[6] Huang, H. and W. Zhang, "Research on the design of hybrid energy storage system for electric vehicles based on built-in permanent magnet motor drive," *China Journal of Construction Machinery*, Vol. 18, No. 1, 68–73, 2020.

[7] Tikadar, A., N. Kumar, Y. Joshi, and S. Kumar, "Coupled electro-thermal analysis of permanent magnet synchronous motor for electric vehicles," in *2020 19th IEEE Intersociety Conference on Thermal and Thermomechanical Phenomena in Electronic Systems (ITherm)*, 249–256, Orlando, FL, USA, 2020.

[8] Li, Q., C. Sun, T. Fan, X. Wen, and Y. Li, "Optimized design of rotor poles for automotive double-layer embedded permanent magnet motors," *Journal of Electrical Machines and Control*, Vol. 24, No. 9, 56–64, 2020.

[9] Parsapour, A., M. Moallem, I. Boldea, and B. Fahimi, "High torque density double stator permanent magnet electric machine," in *2019 IEEE International Electric Machines & Drives Conference (IEMDC)*, 664–670, San Diego, CA, USA, 2019.

[10] Wu, J., Y. Hu, B. Zhang, G. Feng, and Z. Liu, "Comparison and analysis of different rotor structures of double-stator permanent magnet synchronous motor," *IET Electric Power Applications*, Vol. 16, No. 6, 685–700, 2022.

[11] Chai, F., J. Xia, B. Guo, and S. Cheng, "Double-stator permanent magnet synchronous in-wheel motor for hybrid electric drive system," in *2008 14th Symposium on Electromagnetic Launch Technology*, 1–5, Victoria, BC, Canada, 2008.

[12] Wang, D., D. Zhang, D. Xue, C. Peng, and X. Wang, "A new hybrid excitation permanent magnet machine with an independent AC excitation port," *IEEE Transactions on Industrial Electronics*, Vol. 66, No. 8, 5872–5882, 2018.

[13] Zhao, X. and T. Dong, "Design and electric/generation state analysis of double-stator permanent magnet starter generator," *Electrotechnology*, No. 21, 223–226+230, 2022.

[14] Zhao, Y., W. Huang, W. Jiang, X. Lin, and X. Wu, "Optimal design and performance analysis of dual-stator permanent magnet fault-tolerant machine," *IEEE Transactions on Magnetics*, Vol. 57, No. 2, 1–6, 2021.

[15] Gu, S., "Research on magnetic coupling analysis and optimal design of heteropolar double-stator permanent magnet synchronous motor," Ph.D. dissertation, Qingdao University, Qingdao, China, 2022.

[16] Bilal, M., J. Ikram, A. Fida, S. S. H. Bukhari, N. Haider, and J.-S. Ro, "Performance improvement of dual stator axial flux spoke type permanent magnet vernier machine," *IEEE Access*, Vol. 9, 64 179–64 188, 2021.

[17] Kim, D., H. Hwang, S. Bae, and C. Lee, "Analysis and design of a double-stator flux-switching permanent magnet machine using ferrite magnet in hybrid electric vehicles," *IEEE Transactions on Magnetics*, Vol. 52, No. 7, 1–4, 2016.

[18] Ahmad, M. S., D. Ishak, T. T. Leong, and M. R. Mohamed, "Analytical subdomain model for double-stator permanent magnet synchronous machine with surface-mounted radial magnetization," *Engineering Proceedings*, Vol. 12, No. 1, 37, 2021.

[19] Tarek, M. T. B., S. Das, and Y. Sozer, "Comparative analysis of static eccentricity faults of double stator single rotor axial flux permanent magnet motors," in *2019 IEEE Energy Conversion Congress and Exposition (ECCE)*, 3223–3228, Baltimore, MD, USA, 2019.

[20] Wang, Z., D. Wang, C. Wang, *et al.*, "Basic mechanism and operating characteristics of a new AC magnetically regulated permanent magnet synchronous motor," *Chinese Journal of Electrical Engineering*, Vol. 43, No. 7, 2573–2585, 2023.

[21] Xia, Y., W. Gong, S. Huang, *et al.*, "Effect of fundamental armature magnetokinetic potential on rotor tooth harmonic electric potential," *Chinese Journal of Electrical Engineering*, Vol. 35, No. 9, 2304–2309, 2015.

[22] Xia, Y., S. Zhong, L. Zhou, Z. Wen, Y. Chen, and J. Zhang, "Influence of design parameters on the field current of the tooth harmonic excitation system," *IET Electric Power Applications*, Vol. 14, No. 9, 1702–1711, 2020.

[23] Cui, X., "Electromagnetic design and analysis of built-in tangential permanent magnet synchronous generator," Ph.D. dissertation, Harbin Institute of Technology, Harbin, China, 2015.

[24] Qu, C., Z. Guo, Y. Hu, X. Wang, and F. Han, "Multi-objective optimization design of a new permanent magnet synchronous motor based on the Taguchi method," *Energies*, Vol. 15, No. 19, 7347, 2022.

[25] Si, J., S. Zhao, H. Feng, R. Cao, and Y. Hu, "Multi-objective optimization of surface-mounted and interior permanent magnet synchronous motor based on Taguchi method and response surface method," *Chinese Journal of Electrical Engineering*, Vol. 4, No. 1, 67–73, 2018.

[26] Xu, J., L. Gao, L. Zeng, and R. Pei, "Optimum design of interior permanent magnet synchronous motor using Taguchi method," in *2019 IEEE Transportation Electrification Conference and Expo (ITEC)*, 1–4, Detroit, MI, USA, 2019.